Environmental Science: Atmospheres

ROYAL SOCIETY OF CHEMISTRY

PAPER

View Article Online
View Journal

Cite this: DOI: 10.1039/d6ea00006a

Pre-existing particle composition controls the initial viscosity and aging of α-pinene-derived secondary organic aerosol

Katherine R. A. Kolozsvari, [a] Natasha M. Garner, *[bc] David M. Bell, [b] Jens Top, [b] Markus Ammann [b] and Andrew P. Ault *[a]

Secondary organic aerosol (SOA) is a significant contributor to the global burden of fine particulate matter, which impacts both climate and health. α-Pinene is a widely-studied volatile organic compound (VOC) with high global emissions and SOA-forming potential. However, the vast majority of SOA forms on preexisting particles whose composition leads to different molecular species and physical properties. Understanding the viscosity of SOA-containing particles is critical to predicting their atmospheric behavior, as it influences heterogeneous chemistry, particle growth, and particle aging. The viscosity of SOA can range over many orders of magnitude from liquid (<10^2 Pa s) to viscous to glassy (>10^{12} Pa s). Nanothermal analysis (NanoTA) measures single particle melting temperatures (T_m) for submicron particles, which can be converted to glass transition temperatures (T_g), viscosities, and, ultimately, mixing time scales. In this study, we directly measured the T_m of α-pinene SOA formed with no seeds, ammonium sulfate seeds, and Fe-containing ammonium sulfate seeds, both before and after UV exposure. We compare these to modeled viscosities based on chemical composition measurements of the bulk aerosol. The median viscosity of measured particles was 1–3 orders of magnitude more viscous than predicted by existing models for all conditions except those of freshly-emitted, unseeded SOA. After UV exposure, the T_m values for all seed conditions converged, indicating that aged SOA viscosity was less dependent on the initial seed. These results indicate the importance of pre-existing seed particles for initial SOA viscosity and that this viscosity evolves during a particle's atmospheric lifetime.

Received 12th January 2026
Accepted 5th March 2026

DOI: 10.1039/d6ea00006a

rsc.li/esatmospheres

Environmental significance

Secondary organic aerosol (SOA) is a large and difficult to control source of atmospheric particulate matter (PM) that is commonly internally mixed with inorganic components from both anthropogenic and natural sources. Interactions between inorganic and organic components can alter the physical and chemical properties within SOA-containing particles, including viscosity, which impacts particle aging through heterogeneous chemical reactions by altering mixing timescales. We show that particle viscosity depends on initial particle presence, composition, and UV aging through direct measurements of the melting temperature (T_m) of submicron α-pinene-derived SOA formed from nucleation or uptake onto inorganic seed particles (ammonium sulfate with and without iron). Viscosities from T_m measurements and chemical composition-based predictions only agreed in the case of unseeded, unaged SOA.

Introduction

Fine particulate matter, or particulate matter less than 2.5 μm ($PM_{2.5}$), is a class of air pollution with global impacts on climate through direct (absorbing and scattering solar radiation)[1] and indirect (cloud condensation and ice nucleation)[2] effects. Additionally, exposure to $PM_{2.5}$ is associated with adverse health outcomes.[3] Due in part to the physical and chemical heterogeneity of $PM_{2.5}$,[4] it remains the largest source of uncertainty in global models predicting radiative forcing.[5] Secondary organic aerosol (SOA) is formed after the oxidation of volatile organic compounds (VOCs), which causes a decrease in volatility, allowing for reactive uptake or condensation of these lower volatility species onto pre-existing particles.[6] SOA accounts for a significant fraction of $PM_{2.5}$ mass globally.[7] SOA particles are chemically complex, and differences in chemical composition play a major role in determining particle viscosity, through impacts of different functional groups, oxygenation, and the degree of oligomerization.[8–12]

The viscosity of SOA is an important metric to quantify, as it impacts the behavior of particles in terms of chemical reactivity, particle growth, photochemistry, and aging.[13–17] Generally, more

[a]Department of Chemistry, University of Michigan, Ann Arbor, Michigan 48109, USA. E-mail: aulta@umich.edu

[b]PSI Center for Energy and Environmental Sciences, Paul Scherrer Institute, Villigen 5232, Switzerland. E-mail: n.m.garner@leeds.ac.uk

[c]School of Chemistry, University of Leeds, Leeds, West Yorkshire, LS2 9JT, UK

viscous particles experience chemical mixing on a slower timescale due to diffusional limitations, with the e-folding equilibration time for 100 nm diameter semi-solid particles ranging over 10 orders of magnitude, from ~100 ms (10^2 Pa s) to ~10 years (10^{12} Pa s).[13] The chemical mixing timescales for more viscous SOA can therefore be much longer than a particle's atmospheric lifetime. In addition, photochemistry and viscosity are intertwined; a higher particle viscosity can increase the chemical lifetime of radicals and reactive oxygen species,[16] and exposure to UV radiation can increase the viscosity of SOA by multiple orders of magnitude.[17] All of these factors are important considerations when modeling particle behavior over time.

Monoterpenes are an important class of biogenic VOCs (BVOCs) that lead to significant SOA formation,[18] and of these, α-pinene is the monoterpene with the greatest emissions.[19] Previous studies demonstrate that SOA formed from α-pinene oxidation under 80% RH has a viscosity in the semi-solid (10^2–10^{12} Pa s) or solid (>10^{12} Pa s) range.[20–23] Additional work has shown that the presence of pre-existing aerosol (*i.e.*, seed particles) greatly impacts the molecular composition of the SOA, with SOA formed at a high (>80%) RH with ammonium sulfate (AS) seed particles forming a higher fraction of oligomers relative to SOA formed through self-nucleation.[24] In addition to altering the molecular composition of the organic fraction, the presence of inorganic components within SOA will impact the material properties of the particle as a whole, including viscosity, based both on the properties of the inorganic material itself and interactions between the inorganic and organic components.[25,26] Typically, SOA is internally mixed with inorganic species at the single particle level,[4,27,28] including sulfate, ammonium, and nitrate.[29,30] SOA can also be internally mixed with other inorganic species, including iron,[31,32] which can form organic complexes,[33] promote oligomer formation,[34] and serve as a sink for carboxylates.[35] The presence of Fe within AS seeds also affects the chemistry of SOA formed through increased dimerization, as well as enhanced fragmentation reactions during dark aging.[34] Fe-induced photochemistry also has the potential to change the composition of SOA.[36,37] Both dark and photochemically induced chemistry directly impacts the particle viscosity of the SOA formed, as chemical composition is an important factor determining particle viscosity.[13]

There are many methods used to determine the viscosity of SOA materials, and their applicability depends on particle size and viscosity.[38,39] However, most techniques are limited to the supermicron size regime, including bead mobility, poke flow, hot-stage microscopy, and optical tweezing.[20,40–42] This size-range is much larger than the size of typical SOA particles which are generally on the order of 100 nm in diameter. Furthermore, SOA often forms complex morphologies (*e.g.*, core–shell, partially-engulfed), which can be altered when larger supermicron particles are formed *via* coagulation of SOA particles, highlighting the importance of submicron measurements to study individual particle viscosity.

Atomic force microscopy (AFM) allows for direct analysis of the physical properties of particles with nanoscale resolution. Currently, multiple AFM-based techniques measure phase behavior and transitions for individual, submicron particles.[43–46] These can account for particle-to-particle variability within a population, overcoming the limitations of bulk measurements of viscosity. Force-curve measurements can ascertain the viscosities of semi-solid particles between ~10^4 and 10^7 Pa s,[45] and can determine phase transition relative humidities (RHs).[43] Nanothermal analysis (NanoTA) can determine the melting temperature (T_m) for particles between 30 and 300 °C,[46,47] which can then be used to calculate viscosities based on established conversions.[13] As NanoTA measurements are conducted under dry conditions, they can allow for disambiguation between the impacts of temperature and RH on particle phase transitions, elucidating intrinsic composition-based properties.

Previous studies have derived predictions of glass transition temperatures (T_g) of compounds based on their chemical formulae,[48,49] allowing for T_g predictions from the bulk chemical composition of SOA measured with mass spectrometry.[17,47] Similarly to T_m measurements, T_g predictions can be converted to viscosities and mixing timescales through these established methods.[13] However, questions remain about the relationships between mixing timescales calculated from single particle (AFM-based) measurement and connecting these measurements to ensemble average data (*e.g.*, mass spectrometry of bulk samples).

This study determines the viscosity of SOA formed from ozonolysis of α-pinene on different seed particles (or unseeded) in the dark, both before and after UV aging. Unseeded, AS seeded, and Fe-containing AS (Fe/AS) seeded SOA were analyzed with NanoTA to measure the T_m of individual particles directly, and with extractive electrospray ionization time-of-flight mass spectrometry (EESI-TOFMS) to predict the viscosity based on bulk chemical composition. With these measurements, the influence of chemical composition on particle viscosity is highlighted, as neither method takes into account the particle liquid water content (LWC) during the initial measurements, allowing for differentiation between the impacts of RH and composition on particle viscosity. These measurements revealed a convergence of particle T_m after UV aging, indicating that under well-mixed (high RH) conditions seed composition is an important factor to consider when determining the impact of aging mechanisms on particle viscosity, which likely varies based on the elapsed time a particle spends in the atmosphere.

Experimental

Secondary organic aerosol (SOA) generation

Experiments were conducted in an 8 m^3 Teflon chamber operated in batch mode at the Paul Scherrer Institute, Switzerland,[50,51] in accordance with previous experiments.[24,34] The chamber was housed in a temperature-controlled shipping container with temperature maintained at 21 ± 1 °C. Prior to each experiment, the chamber was flushed overnight with dry, VOC, and NO_x-free air at 50 L min^{-1} from an air generator (737–250 series, AADCO Instruments, Inc., USA) to ensure a clean starting condition. The chamber was humidified to >90% RH at the start of each experiment using zero air humidified by

passing it through a 2 L heated round-bottom flask filled with 18.2 MΩ cm Milli-Q water. The RH was monitored using an RH probe (Vaisala, model 3938, TSI Inc.). For seeded experiments, the inorganic seed solution was nebulized producing an aerosol mass concentration of ~70 μg m^{-3} as monitored with a scanning mobility particle sizer (SMPS model 3938, TSI Inc.), assuming a particle density of 1.2 g cm^{-3}. Ammonium sulfate (AS) seed particles were nebulized with a solution of 3 g L^{-1} $(NH_4)_2SO_4$ (Sigma-Aldrich, ≥99%) in 18.2 MΩ cm Milli-Q water. Iron-containing ammonium sulfate (Fe/AS) seed solutions were created by nebulizing a solution of equivalent volumes of the 3 g L^{-1} $(NH_4)_2SO_4$ solution described above and 5 g L^{-1} iron(II) sulfate in 18.2 MΩ cm Milli-Q water. Fe/AS seed solutions were prepared immediately before each experiment and were shielded with foil to prevent photochemical reactions and minimize oxidation reactions.

After injecting seed particles for seeded experiments, or after RH conditioning for unseeded experiments, 300 ppbv of O_3 was added by flowing dry air through a UV lamp (λ = 254 nm). O_3 concentration was continuously monitored throughout each experiment with a multi-gas analyzer (MIRO, MGA[10]-GP). Following O_3 addition, 3.2 μL of α-pinene (TCI, > 97.0% by mass) was injected *via* a syringe through a heated (80 °C) septum into the chamber and flushed at ~60 L min^{-1}. Fresh SOA microscopy samples were collected ~1 hour after α-pinene injection. To simulate aging, a set of 40 UV lights (90–100 W, peak emission 368 nm, Cleo Performance, Philips)[50] under the chamber were illuminated for 1 hour, beginning 3 hours after α-pinene injection. Post-photolysis microscopy samples were collected immediately after the UV lights were turned off. The basic setup of the chamber and experimentation configuration is shown in Fig. 1.

Microscopy sample collection

Microscopy samples were collected with a mini micro-orifice uniform deposit impactor (mini-MOUDI, 135-10B, TSI Inc.). Samples were collected onto silicon substrates (Ted Pella, Inc.) on stage 9 (d_{50} = 0.18 μm) for ~10 min. Once collected, samples were placed in individual plastic containers and wrapped in parafilm and foil to prevent light exposure. The samples were stored at −20 °C until analysis to minimize chemical changes before T_m analysis. This is not typically recommended for microscopy analysis as it can alter particle morphology;[52] however, it was chosen in this case since T_m is highly impacted by chemical composition.

Atomic force microscopy (AFM) analysis

Microscopy samples were analyzed using nanothermal analysis (NanoTA), a technique previously employed to determine the T_m of individual aerosol particles.[46,47] As has been done previously for organic particles,[46,47] samples were analyzed under dry (RH < 5%) conditions. This is done to ensure consistency across samples and to ensure that all particles are initially in a solid state for analysis. Water content from the initial RH of formation is taken into account during viscosity calculations. Thermal AFM tips (Bruker Nano, Inc., Model: PR-Exp-AN2-200) were operated in contact mode at a heating rate of 1 °C s^{-1} and were calibrated using polyethylene terephthalate (PET, T_m = 235 °C), high-density polyethylene (HDPE, T_m = 116 °C), and polycaprolactone (PCL, T_m = 55 °C). The majority of samples were analyzed at the University of Michigan with an upgraded NanoIR2 AFM system (Bruker Nano, Inc.) within a month of collection; however, a small subset of samples were analyzed ~1 year after collection with a NanoIR3 system (Bruker Nano, Inc.) at Sandia National Laboratories (Albuquerque, New Mexico) due to the NanoIR2 at Michigan not functioning. A complete list of experiment and sample analysis dates, including the number of particles analyzed per sample, is available in the SI (Table S1). The T_m measurements separated by experiment for replicate experiments under the same conditions are also available in the SI (Fig. S1). The NanoTA probe was cleaned every ~10 ramps by heating to 250 °C for 0.5 s. For NanoTA curves with multiple

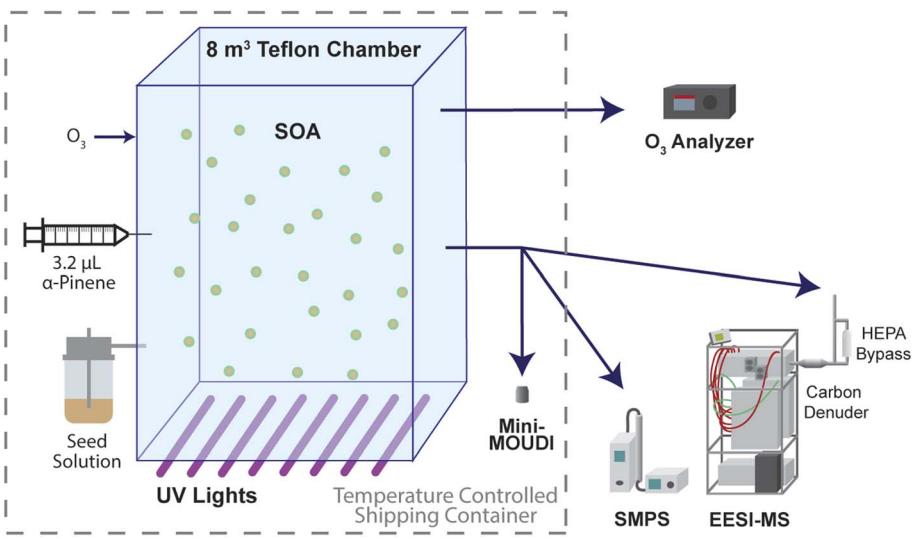

Fig. 1 Diagram of the chamber and instrumentation setup. After the injection of SOA precursors, the chamber was operated in batch mode.

features, the feature with the lowest temperature was assigned as the T_m.

Online aerosol measurements

Particle size distributions were monitored continuously using an SMPS (TSI, Inc., Model 3082 Electrostatic Classifier, Model 3750 Condensation Particle Counter). The SMPS measurements were performed behind a Nafion™ drier to consistently determine the dry diameter of the particles in the chamber. The bulk chemical composition of the aerosol was monitored with an extractive electrospray ionization time-of-flight mass spectrometer (EESI-TOFMS, Tofwerk), with a home-built EESI inlet coupled to an atmospheric pressure interface time-of-flight mass spectrometer (Api-TOF; Tofwerk AG).[53,54] The aerosol was sampled at a flow rate of 0.8 L min^{-1} through an extruded carbon denuder (Ionicon, in custom holder) to remove gas phase components. The electrospray solution was composed of 100 ppm NaI in 18.2 MΩ cm Milli-Q water. Mass spectra were collected in positive ion mode at 1 Hz, and all ions were detected as adducts with Na^+.

Data analysis for EESI-TOFMS was conducted with Tofware version 4.0.0 (Tofwerk AG, Thun, Switzerland). Data were averaged to 10 s before peak fitting was performed. Fitted peaks were assigned molecular formulae up to C_{20}. Background measurements were taken at 90 s intervals after 5 min of sample measurement (6.5 min total cycle) by alternating between chamber air and HEPA-filtered chamber air.

Viscosity calculations

NanoTA directly measures T_m of the dry particle, so direct measurements were first converted to T_g using the Boyer–Beaman rule (eqn (1)),[55]

$$T_g = g \times T_m \quad (1)$$

assuming $g = 0.7$ based on empirical data for SOA compounds.[13] This assumption is therefore carried through to calculations of viscosity for NanoTA measurements. For predictions of viscosity based on EESI-TOFMS data, the T_g of each measured compound was predicted from chemical composition using the model for CHO compounds described in DeRieux *et al.*[48] To represent the glass transition of the organic–water mixture, $T_{g,mix}$, the Gordon–Taylor equation was used as has been done previously,[13,56]

$$T_{g,mix} = \frac{(1 - w_{org})T_{g,w} + \frac{1}{k_{GT}} w_{org} T_{g,org}}{(1 - w_{org}) + \frac{1}{k_{GT}} w_{org}} \quad (2)$$

where k_{GT} is the Gordon–Taylor constant, assumed to be 2.5 for this system,[56] and $T_{g,org}$ represents either the T_g of the SOA material calculated from NanoTA T_m measurements or the average T_g of the organic components predicted based on their chemical formulae and weighted based on their prevalence in EESI-TOFMS spectra. The EESI-TOFMS peak abundances were corrected for the effects of molecular weight (MW) and degree of unsaturation on ionization efficiency based on previous work,[22,57]

$$w_i = \frac{PA_i}{(H:C)_i \times MW_i} \quad (3)$$

where PA_i is the peak area of an individual compound and $(H:C)_i$ is the hydrogen to carbon ratio for an individual compound. The mass fraction of organics, w_{org}, is calculated as:

$$w_{org} = \left(1 + \kappa\left(\frac{a_w}{1 - a_w}\right)\right)^{-1} \quad (4)$$

where a_w is the activity of water and κ is the mass-based hygroscopicity parameter.[58] For this work, we assumed a volume-based hygroscopicity parameter of 0.1 and a particle density of 1.3 g cm^{-3}, giving a κ of 0.077.[59]

From $T_{g,org}$, the viscosity of the system at a given temperature, T, can be calculated based on the modified Vogel–Tammann–Fulcher (VTF) equation,[17,48]

$$\eta = \eta_\infty e^{\frac{T_0 D_{frag}}{T - T_0}} \quad (5)$$

where η_∞ is the viscosity at an infinite temperature, assumed to be 10^{-5} Pa s,[17,60] D_{frag} is the fragility parameter assumed here to be 10,[48] and T_0 is a fitted parameter corresponding to the temperature at which the viscosity begins to approach infinity asymptotically.[58] Since this work is not directly measuring viscosity, T_0 is calculated by rearranging eqn (5) under the assumption that the viscosity at the glass transition is 10^{12} Pa s as has been done previously:[15,17,39,49]

$$T_0 = \frac{\ln\left(\frac{10^{12}}{\eta_\infty}\right) T_{g,mix}}{D_{frag} + \ln\left(\frac{10^{12}}{\eta_\infty}\right)} \quad (6)$$

It is worth noting that there are materials with lower viscosities at the glass transition, especially in cases of fragile systems, which are characterized by a deviation from Arrhenius behavior.[61]

Viscosities can be used to determine molecular self-diffusion coefficients (D_{org}), through the Stokes–Einstein equation:[15]

$$D_{org} = \frac{kT}{6\pi\eta R_{diff}} \quad (7)$$

where k is the Boltzmann constant and R_{diff} is the hydrodynamic radius of the organic molecule, calculated here to be 3.9×10^{-10} m assuming spherical geometry, a density of 1.3 g cm^{-3}, and a molar mass of 200 g mol^{-1}. From D_{org}, characteristic mixing time scales (τ), defined as the time period required for the concentration of the diffusing molecule to deviate from equilibrium concentration by less than $1/e$, can be calculated:[15]

$$\tau = \frac{{d_p}^2}{4\pi^2 D_{org}} \quad (8)$$

with d_p representing the aerosol particle diameter.

Results and discussion

A series of chamber experiments were conducted to determine the impacts of seed particles and UV aging on SOA viscosity. The aerosol mass concentration was measured with an SMPS over the course of the experiments. In a typical experiment, microscopy samples of fresh SOA were collected 1–2 hours after α-pinene injection, and UV aged samples were collected immediately after UV exposure. Information regarding the conditions for every experiment is included in the SI (Table S1). The SMPS traces were corrected for wall loss semi-empirically based on the first-order decay from the peak of SOA mass formation until ~2 hours after α-pinene injection. The average aerosol mass during the periods of microscopy sample collection is given in Fig. 2. For seeded experiments, the peak concentration of seeds before α-pinene injection is shown in gray. Although all seed conditions observed mass loss with UV aging, SOA with Fe/AS seeds had a far greater reduction in total aerosol mass under UV exposure (Fig. 2), likely due to the photoactivity of iron complexes.[35,62] This means that after UV aging, the ratio of inorganic to organic material is highly shifted toward inorganic seeds for the Fe/AS seeded experiments.

Microscopy samples for single-particle analysis were collected under both fresh (pre-UV exposure) and UV aged (immediately post-UV exposure) conditions. These samples then were analyzed with NanoTA to determine the T_m of individual particles, a technique previously used for analysis of chamber-generated SOA.[47] Briefly, this method utilizes a resistively heated AFM probe that sinks into the sample when it reaches its T_m (Fig. 3A). The heating is localized, and representative AFM height images from each sample demonstrate the divots formed as the tip sinks into the particle during NanoTA. Although there does appear to be a difference in particle morphology for the Fe/AS seeded particles (Fig. 3F and G), this is likely due to the storage conditions before analysis and should not be interpreted as a significant finding. As this work is concerned with the impacts of particle composition on viscosity, samples were frozen immediately after collection to prevent changes in chemical composition over time; however, it is known that freeze–thaw cycles can impact the morphology of organic aerosol particles.[52] Immediately before NanoTA analysis the particles were dried under N_2 for NanoTA measurements.

For freshly formed SOA, most particles from both seeded SOA conditions had higher T_m values than the unseeded SOA, and the Fe/AS seeded SOA had higher T_m values than the AS seeded SOA (Fig. 4A). However, a large spread (over 100 °C) exists for all conditions, indicating that there is a large amount of particle-to-particle variation in T_m, despite formation under identical conditions. This indicates particle-to-particle variability in chemical composition, which is an important consideration as bulk analysis will not capture this

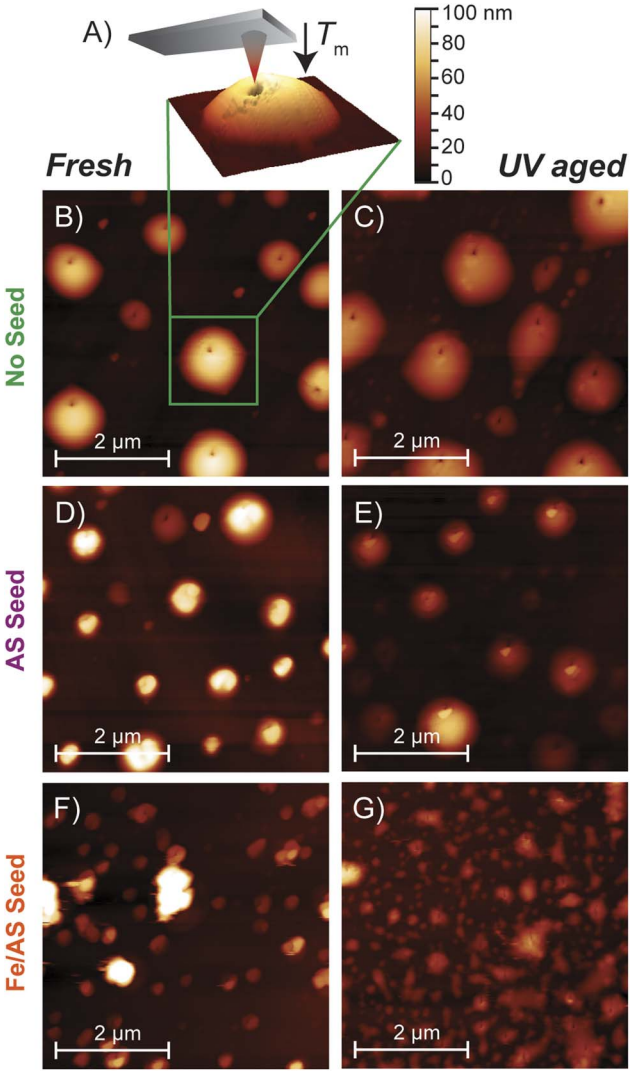

Fig. 3 (A) A 3D AFM height image of a particle after NanoTA with a cartoon depiction of an AFM tip above the indentation caused during heating. (B–G) AFM height images of each sampling condition: unseeded fresh, unseeded UV aged, AS seeded fresh, AS seeded UV aged, Fe/AS seeded fresh, and Fe/AS seeded UV aged, respectively.

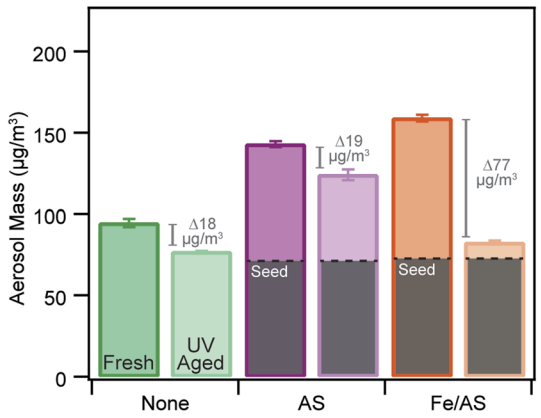

Fig. 2 The average wall-loss corrected aerosol mass for fresh (1–2 h after α-pinene injection) and UV aged (>4 h after α-pinene injection) SOA. Peak concentrations of seeds are indicated with a dashed line for the seeded experiments. The wall-loss corrected difference in aerosol mass with UV aging is indicated in gray. Error bars represent the standard deviation in aerosol mass over the time period sampled. The error associated with the wall loss correction is not included.

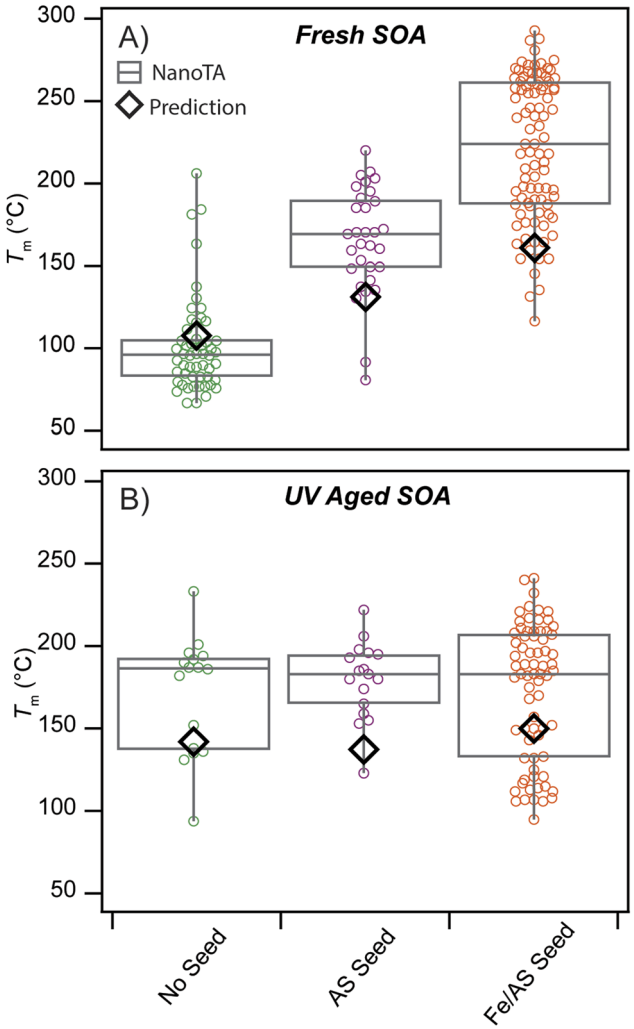

Fig. 4 NanoTA measurements (boxplots) and chemical composition-based predictions (diamonds) of T_m for (A) fresh SOA (no UV exposure) and (B) UV aged SOA for unseeded, AS seeded, and Fe/AS seeded SOA. Each colored marker represents an individual particle measurement. The interquartile range and median values are visualized in gray as box plots.

phenomenon. Using Welch's unequal variance *t*-test, the average T_m for fresh AS seeded SOA is significantly larger than the average T_m for fresh unseeded SOA (t statistic = 9.20, degrees of freedom = 57) and the average T_m for fresh Fe/AS seeded SOA is significantly larger than the average T_m for fresh AS seeded SOA (t statistic = 7.71, degrees of freedom = 69). This general trend of increasing viscosity with seeds, highest for Fe/AS seeds, is in line with previous work showing increased dimer formation in AS seeded SOA as opposed to unseeded SOA,[24] and increased dimer formation in Fe/AS seeded SOA as opposed to AS seeded SOA 1 h after α-pinene injection.[34] After UV aging, the median T_m values for all conditions converged to ~185 °C, although the wide spread in values remains post-UV aging (Fig. 4B). The increase in T_m for the unseeded condition is expected based on previous research of the impacts of UV aging on SOA viscosity;[17] however, the effects on T_m for the seeded conditions were surprising. Predictions of T_m based on the bulk chemical composition measured by EESI-TOFMS generally follow the same trends as the NanoTA measurements, although they underpredict T_m in most cases (Fig. 4). These predictions are initially made as T_g values and are converted to T_m based on the Boyer–Beaman rule (eqn (1)).

With EESI-TOFMS, the relative contributions of monomers and dimers were measured to determine the chemical reasons for the trends observed in T_m. For the unseeded SOA, there was a relative decrease in monomer abundance and an increase in dimer abundance with UV aging (Fig. 5, left), associated with an increase in predicted SOA viscosity (Fig. 4). For the AS seeded SOA, there is a slight relative decrease in monomer abundance with UV aging (Fig. 5, middle), which predicts a slight increase in viscosity. For Fe/AS seeded SOA, the relative monomer concentration decreases with UV aging; however, the most abundant dimers shift to lower C-number dimers, which is associated with a slight decrease in SOA viscosity (Fig. 5, right). It has been shown previously that the functionality of these compounds is also shifting, with fewer carboxylic acid and alkane species and more alcohol species after UV aging of Fe/AS seeded SOA.[37]

The viscosity of the SOA particles was calculated based on the measured NanoTA T_m values,[47] while the model-predicted viscosity was calculated from the chemical composition measured by EESI-TOFMS.[48] From this, we observe that for all conditions other than the unseeded fresh SOA, the model based on EESI-TOFMS underpredicts the viscosity measured by NanoTA (Fig. 6A and B). For the seeded conditions, this may be partly due to the fact that EESI-TOFMS may not effectively measure molecules containing an organosulfate functional group and therefore may not capture all organic material present. Additionally, predicting the viscosity of SOA solely based on the organic material will not account for interactions between inorganic and organic species (*e.g.*, formation of iron–organic complexes), which may change the overall viscosity of the particle. The viscosity calculated from NanoTA measurements increases across all seed conditions, mainly due to a decrease in RH over the course of the batch experiment. This

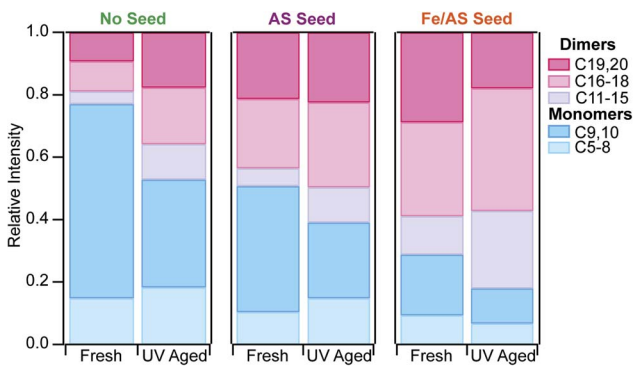

Fig. 5 Bar graphs demonstrating the average chemical composition measured by EESI of the SOA from unseeded, AS seeded, and Fe/AS seeded experiments. These compositions are from the time periods that microscopy samples were collected for both fresh and UV aged SOA. Compounds are combined by their carbon content as indicated, with monomers depicted in blue and dimers depicted in pink.

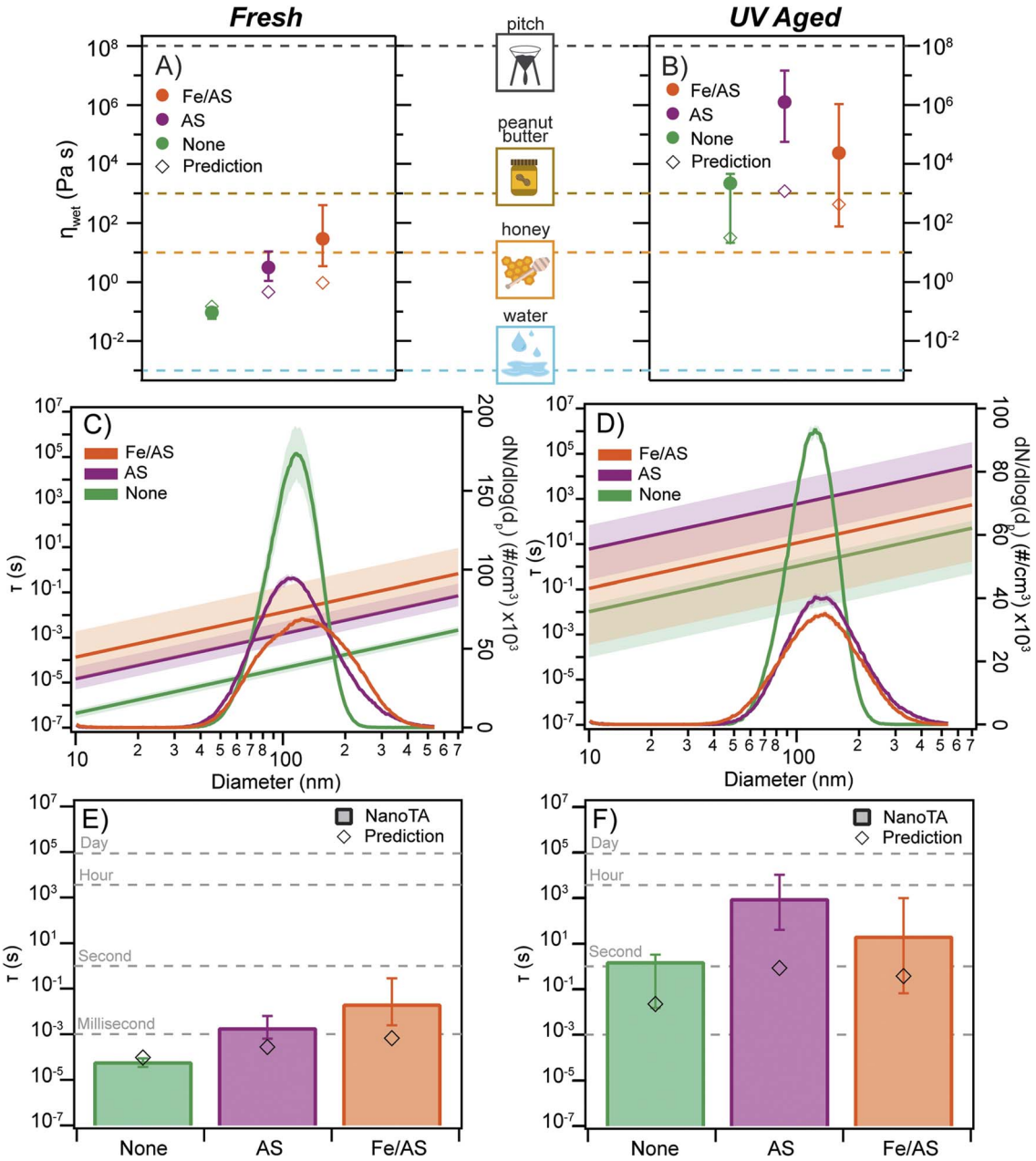

Fig. 6 (A) Fresh, and (B) UV Aged SOA viscosity calculated from NanoTA measurements (solid circles) and EESI-MS chemical composition (open diamonds). The marker for NanoTA measurements is calculated based on the median NanoTA measurement, and the error bars are calculated from the first and third quartile of the dataset. Dotted lines indicating the viscosities of common materials are shown for reference across A and B. (C) Fresh, and (D) UV aged SOA characteristic self-diffusion timescales (diagonal lines) calculated from NanoTA measurements across relevant particle diameters. The particle size distribution during sample collection time measured *via* an SMPS is overlaid. (E) Fresh, and (F) UV aged SOA characteristic self-diffusion timescales at the number mode of the particle size distribution (~100 nm). Day, hour, second, and millisecond are shown as dotted lines for reference.

decrease in RH was not equivalent across experiments (Table S1), which explains the larger increase in viscosity for the AS seeded experiment. Viscosity predictions based on EESI-TOFMS chemical composition exhibit the same trends, although the changes are less extreme. The viscosity and size of a particle dictate the timescale that a molecule can travel through a particle, here indicated by τ, which is the time required for the concentration of a diffusing molecule at the center of the particle to deviate from equilibrium concentration by less than $1/e$.[15] The τ of a 200 g mol^{-1} generic spherical organic molecule with a density of 1.3 g cm^{-3} is shown for relevant particle diameters based on the viscosity calculated from NanoTA measurements (Fig. 6C and D). Overlaid average SMPS number size distribution during sample collection times demonstrates that the most prevalent particle sizes are between 50 and 200 nm in electrical mobility diameter (d_m) for unseeded SOA, and

between 50 and 400 nm in d_m for seeded SOA. The τ for particles with a size at the mode of the SMPS number distribution, calculated based on NanoTA measurements (bars) and chemical composition predictions (diamonds), is shown in Fig. 6E and F, indicating that at the number mode, τ ranges approximately seven orders of magnitude from under a millisecond to almost an hour under the conditions sampled here.

Conclusions

SOA in the atmosphere forms on pre-existing particles (except at the beginning of a nucleation event), and the chemical composition of these seed particles is critical to consider when attempting to predict physicochemical properties. It is well known that SOA is typically internally mixed with inorganic salts within individual particles in the atmosphere.[27,63–67] However, understanding the viscosity of internally mixed inorganic/organic aerosol is challenging, as bulk measurement techniques cannot capture the unique environment present in single particles, and few techniques exist which can determine the viscosity of individual submicron particles. Additionally, water has a large impact on particle viscosity due to its plasticizing properties, making it challenging to separate the effects of chemical composition and water content on particle viscosity.

Herein, we have shown that the presence and composition of inorganic seed particles fundamentally change the chemistry that occurs within SOA particles and their viscosity both before and after aging. Through NanoTA analysis, the T_m of individual, submicron SOA can be determined. With this technique, we demonstrated that the presence of inorganic seeds increased the T_m of α-pinene derived SOA significantly, with Fe/AS seeded particles having a higher T_m than AS seeded particles. After UV aging, the T_m decreased for Fe/AS seeded SOA, increased for unseeded SOA, and stayed similar for AS seeded SOA, with all seed conditions converging around 185 °C. This indicates that chemical reactions and interaction with UV light during the aging processes observed here are dependent on seed composition as there was not a uniform change in T_m with UV aging. Since NanoTA probes from the outermost layer of the particle, it provides the T_m relevant to what is first encountered by other molecules within the atmosphere (*i.e.*, oxidants, semivolatile species). By using EESI-TOFMS analysis, we demonstrate that the T_m trends observed by NanoTA are indeed likely based on changes in chemical composition, as the same trends are also present when predicting T_m using EESI-TOFMS data. However, the predicted T_m's are lower than the median measured data for both seeded and aged conditions, indicating that there are components or interactions not detected by EESI-TOFMS that contribute to the increase in particle T_m. This likely includes both organosulfates and iron–organic complexes (*i.e.*, Fe-carboxylates)[37] which are not detected with EESI-TOFMS. Future studies are needed to explore these differences.

Viscosity calculations demonstrated that for freshly emitted particles, viscosity increased several orders of magnitude for seeded SOA relative to unseeded SOA. Additionally, Fe/AS seeded SOA had a higher initial viscosity than AS seeded SOA by approximately one order of magnitude. After aging, the calculated viscosity of all seed types increased, likely due to the decrease in RH over the course of each batch experiment. The RH decreased by 10–20% over each experiment, as the chamber deflated over time due to continuous sampling. Future work under stable RH conditions is needed to fully determine the impact of compositional changes as opposed to changes in water content for particle viscosity with aging. Overall, understanding the impact of seed compositions on SOA viscosity is important for predicting the long-term behavior of SOA in the atmosphere.

Author contributions

Conceptualization: KRK, NMG, DMB, APA, resources: APA, MA, DMB, investigation: KRK, NMG, DMB, JT, visualization: KRK, APA, DMB supervision: APA, MA writing – original draft: KRK, APA writing – review & editing: all authors.

Conflicts of interest

The authors declare no conflicts of interest.

Data availability

Data for this article are available at the Deep Blue Data repository at https://doi.org/10.7302/sg5a-4845.

Supplementary information (SI): experimental conditions and information on offline analysis (Table S1); T_m measurements split by experiment date for conditions with repeated experiments (Fig. S1). See DOI: https://doi.org/10.1039/d6ea00006a.

Acknowledgements

This work was supported by ATMO-ACCESS Trans-National Access Award ATMO-TNA-5G-0000000126. KRK was supported by the National Science Foundation (NSF) Graduate Research Fellowship DGE-2241144. NMG and MA appreciate funding from the Swiss National Science Foundation (grant no. 188662 and 231265). NMG acknowledges funding from the European Union's Horizon 2020 research and innovation program under the Marie Skłodowska-Curie grant agreement no. 884104. The authors acknowledge Sandia National Laboratories and Dr Ryan Davis for use of their AFM. Funding was also provided under the ATMO-ACCESS Integrating Activity under grant agreement no. 101008004. PSI's atmospheric simulation chamber is a facility of the ACTRIS ERIC and receives funding from the Swiss State Secretariat for Education, Research and Innovation (SERI).

References

1 J. Li, B. E. Carlson, Y. L. Yung, D. Lv, J. Hansen, J. E. Penner, H. Liao, V. Ramaswamy, R. A. Kahn, P. Zhang, O. Dubovik, A. Ding, A. A. Lacis, L. Zhang and Y. Dong, Scattering and absorbing aerosols in the climate system, *Nat. Rev. Earth Environ.*, 2022, **3**, 363–379.

2 U. Lohmann and J. Feichter, Global indirect aerosol effects: a review, *Atmos. Chem. Phys.*, 2005, **5**, 715–737.
3 M. Shiraiwa, K. Ueda, A. Pozzer, G. Lammel, C. J. Kampf, A. Fushimi, S. Enami, A. M. Arangio, J. Fröhlich-Nowoisky, Y. Fujitani, A. Furuyama, P. S. J. Lakey, J. Lelieveld, K. Lucas, Y. Morino, U. Pöschl, S. Takahama, A. Takami, H. Tong, B. Weber, A. Yoshino and K. Sato, Aerosol Health Effects from Molecular to Global Scales, *Environ. Sci. Technol.*, 2017, **51**, 13545–13567.
4 N. Riemer, A. P. Ault, M. West, R. L. Craig and J. H. Curtis, Aerosol Mixing State: Measurements, Modeling, and Impacts, *Rev. Geophys.*, 2019, **57**, 187–249.
5 IPCC, *Climate Change 2021: the Physical Science Basis. Contribution of Working Group I to the Sixth Assessment Report of the Intergovernmental Panel on Climate Change*, Cambridge, United Kingdom and New York, NY, USA, 2021.
6 M. Hallquist, J. C. Wenger, U. Baltensperger, Y. Rudich, D. Simpson, M. Claeys, J. Dommen, N. M. Donahue, C. George, A. H. Goldstein, J. F. Hamilton, H. Herrmann, T. Hoffmann, Y. Iinuma, M. Jang, M. E. Jenkin, J. L. Jimenez, A. Kiendler-Scharr, W. Maenhaut, G. McFiggans, T. F. Mentel, A. Monod, A. S. H. Prévôt, J. H. Seinfeld, J. D. Surratt, R. Szmigielski and J. Wildt, The formation, properties and impact of secondary organic aerosol: current and emerging issues, *Atmos. Chem. Phys.*, 2009, **9**, 5155–5236.
7 M. Kanakidou, J. H. Seinfeld, S. N. Pandis, I. Barnes, F. J. Dentener, M. C. Facchini, R. Van Dingenen, B. Ervens, A. Nenes, C. J. Nielsen, E. Swietlicki, J. P. Putaud, Y. Balkanski, S. Fuzzi, J. Horth, G. K. Moortgat, R. Winterhalter, C. E. L. Myhre, K. Tsigaridis and E. Vignati, Organic aerosol and global climate modelling: a review, *Atmos. Chem. Phys.*, 2005, **5**, 1053–1123.
8 R. Gani, Group contribution-based property estimation methods: advances and perspectives, *Curr. Opin. Chem. Eng.*, 2019, **23**, 184–196.
9 P. Siachouli, V. G. Mavrantzas and S. N. Pandis, Predicting and parameterizing the glass transition temperature of atmospheric organic aerosol components via molecular dynamics simulations, *Soft Matter*, 2025, **21**, 3880–3889.
10 N. E. Rothfuss and M. D. Petters, Influence of Functional Groups on the Viscosity of Organic Aerosol, *Environ. Sci. Technol.*, 2017, **51**, 271–279.
11 Z. Y. Lei, N. E. Olson, Y. Zhang, Y. Z. Chen, A. T. Lambe, J. Zhang, N. J. White, J. M. Atkin, M. M. B. Holl, Z. F. Zhang, A. Gold, J. D. Surratt and A. P. Ault, Morphology and Viscosity Changes after Reactive Uptake of Isoprene Epoxydiols in Submicrometer Phase Separated Particles with Secondary Organic Aerosol Formed from Different Volatile Organic Compounds, *ACS Earth Space Chem.*, 2022, **6**, 871–882.
12 Z. Lei, Y. Chen, Y. Zhang, M. E. Cooke, I. R. Ledsky, N. C. Armstrong, N. E. Olson, Z. Zhang, A. Gold, J. D. Surratt and A. P. Ault, Initial pH Governs Secondary Organic Aerosol Phase State and Morphology after Uptake of Isoprene Epoxydiols (IEPOX), *Environ. Sci. Technol.*, 2022, **56**, 10596–10607.
13 T. Koop, J. Bookhold, M. Shiraiwa and U. Pöschl, Glass transition and phase state of organic compounds: dependency on molecular properties and implications for secondary organic aerosols in the atmosphere, *Phys. Chem. Chem. Phys.*, 2011, **13**, 19238–19255.
14 M. Shiraiwa, A. Zuend, A. K. Bertram and J. H. Seinfeld, Gas–particle partitioning of atmospheric aerosols: interplay of physical state, non-ideal mixing and morphology, *Phys. Chem. Chem. Phys.*, 2013, **15**, 11441–11453.
15 M. Shiraiwa, M. Ammann, T. Koop and U. Pöschl, Gas uptake and chemical aging of semisolid organic aerosol particles, *Proc. Natl. Acad. Sci. U. S. A*, 2011, **108**, 11003–11008.
16 P. A. Alpert, J. Dou, P. Corral Arroyo, F. Schneider, J. Xto, B. Luo, T. Peter, T. Huthwelker, C. N. Borca, K. D. Henzler, T. Schaefer, H. Herrmann, J. Raabe, B. Watts, U. K. Krieger and M. Ammann, Photolytic radical persistence due to anoxia in viscous aerosol particles, *Nat. Commun.*, 2021, **12**, 1769.
17 V. J. Baboomian, G. V. Crescenzo, Y. Huang, F. Mahrt, M. Shiraiwa, A. K. Bertram and S. A. Nizkorodov, Sunlight can convert atmospheric aerosols into a glassy solid state and modify their environmental impacts, *Proc. Natl. Acad. Sci. U. S. A*, 2022, **119**, e2208121119.
18 D. V. Spracklen, J. L. Jimenez, K. S. Carslaw, D. R. Worsnop, M. J. Evans, G. W. Mann, Q. Zhang, M. R. Canagaratna, J. Allan, H. Coe, G. McFiggans, A. Rap and P. Forster, Aerosol mass spectrometer constraint on the global secondary organic aerosol budget, *Atmos. Chem. Phys.*, 2011, **11**, 12109–12136.
19 K. Sindelarova, C. Granier, I. Bouarar, A. Guenther, S. Tilmes, T. Stavrakou, J. F. Müller, U. Kuhn, P. Stefani and W. Knorr, Global data set of biogenic VOC emissions calculated by the MEGAN model over the last 30 years, *Atmos. Chem. Phys.*, 2014, **14**, 9317–9341.
20 L. Renbaum-Wolff, J. W. Grayson, A. P. Bateman, M. Kuwata, M. Sellier, B. J. Murray, J. E. Shilling, S. T. Martin and A. K. Bertram, Viscosity of α-pinene secondary organic material and implications for particle growth and reactivity, *Proc. Natl. Acad. Sci. U. S. A*, 2013, **110**, 8014–8019.
21 Y. Zhang, M. S. Sanchez, C. Douet, Y. Wang, A. P. Bateman, Z. Gong, M. Kuwata, L. Renbaum-Wolff, B. B. Sato, P. F. Liu, A. K. Bertram, F. M. Geiger and S. T. Martin, Changing shapes and implied viscosities of suspended submicron particles, *Atmos. Chem. Phys.*, 2015, **15**, 7819–7829.
22 N. R. Smith, G. V. Crescenzo, Y. Huang, A. P. S. Hettiyadura, K. Siemens, Y. Li, C. L. Faiola, A. Laskin, M. Shiraiwa, A. K. Bertram and S. A. Nizkorodov, Viscosity and liquid–liquid phase separation in healthy and stressed plant SOA, *Environ. Sci.: Atmos.*, 2021, **1**, 140–153.
23 C. Kidd, V. Perraud, L. M. Wingen and B. J. Finlayson-Pitts, Integrating phase and composition of secondary organic aerosol from the ozonolysis of ?-pinene, *Proc. Natl. Acad. Sci. U. S. A*, 2014, **111**, 7552–7557.
24 J. Top, N. M. Garner, F. Sari Doré, Y. Zhang, C. Carstens, C. Dubois, F. Mahrt, M. Ammann, A. S. H. Prévôt, M. Riva, I. El Haddad and D. M. Bell, Influence of Relative

Humidity and Seed Particles on Molecular Composition of α-Pinene Secondary Organic Aerosol, *ACS ES&T Air*, 2025, **2**, 1565–1574.

25 Y. C. Song, J. Lilek, J. B. Lee, M. N. Chan, Z. Wu, A. Zuend and M. Song, Viscosity and phase state of aerosol particles consisting of sucrose mixed with inorganic salts, *Atmos. Chem. Phys.*, 2021, **21**, 10215–10228.

26 D. S. Richards, K. L. Trobaugh, J. Hajek-Herrera, C. L. Price, C. S. Sheldon, J. F. Davies and R. D. Davis, Ion-molecule interactions enable unexpected phase transitions in organic-inorganic aerosol, *Sci. Adv.*, 2020, **6**, eabb5643.

27 A. L. Bondy, D. Bonanno, R. C. Moffet, B. Wang, A. Laskin and A. P. Ault, The diverse chemical mixing state of aerosol particles in the southeastern United States, *Atmos. Chem. Phys.*, 2018, **18**, 12595–12612.

28 M. E. Cooke, C. M. Waters, J. Y. Asare, J. A. Mirrielees, A. L. Holen, M. P. Frauenheim, Z. Zhang, A. Gold, K. A. Pratt, J. D. Surratt, L. A. Ladino and A. P. Ault, Atmospheric Aerosol Sulfur Distribution and Speciation in Mexico City: Sulfate, Organosulfates, and Isoprene-Derived Secondary Organic Aerosol from Low NO Pathways, *ACS ES&T Air*, 2024, **1**, 1037–1052.

29 Y. L. Sun, Q. Zhang, J. J. Schwab, T. Yang, N. L. Ng and K. L. Demerjian, Factor analysis of combined organic and inorganic aerosol mass spectra from high resolution aerosol mass spectrometer measurements, *Atmos. Chem. Phys.*, 2012, **12**, 8537–8551.

30 K. A. Pratt and K. A. Prather, Aircraft measurements of vertical profiles of aerosol mixing states, *J. Geophys. Res.:Atmos.*, 2010, **115**, D11305.

31 R. C. Moffet, H. Furutani, T. C. Rödel, T. R. Henn, P. O. Sprau, A. Laskin, M. Uematsu and M. K. Gilles, Iron speciation and mixing in single aerosol particles from the Asian continental outflow, *J. Geophys. Res.:Atmos.*, 2012, **117**, D07204.

32 H. Furutani, J. Jung, K. Miura, A. Takami, S. Kato, Y. Kajii and M. Uematsu, Single-particle chemical characterization and source apportionment of iron-containing atmospheric aerosols in Asian outflow, *J. Geophys. Res.:Atmos.*, 2011, **116**, D18204.

33 A. Tapparo, V. Di Marco, D. Badocco, S. D'Aronco, L. Soldà, P. Pastore, B. M. Mahon, M. Kalberer and C. Giorio, Formation of metal-organic ligand complexes affects solubility of metals in airborne particles at an urban site in the Po valley, *Chemosphere*, 2020, **241**, 125025.

34 N. M. Garner, J. Top, F. Mahrt, I. El Haddad, M. Ammann and D. M. Bell, Iron-Containing Seed Particles Enhance α-Pinene Secondary Organic Aerosol Mass Concentration and Dimer Formation, *Environ. Sci. Technol.*, 2024, **58**, 16984–16993.

35 C. Weller, A. Tilgner, P. Bräuer and H. Herrmann, Modeling the Impact of Iron–Carboxylate Photochemistry on Radical Budget and Carboxylate Degradation in Cloud Droplets and Particles, *Environ. Sci. Technol.*, 2014, **48**, 5652–5659.

36 J. Dou, P. A. Alpert, P. Corral Arroyo, B. Luo, F. Schneider, J. Xto, T. Huthwelker, C. N. Borca, K. D. Henzler, J. Raabe, B. Watts, H. Herrmann, T. Peter, M. Ammann and U. K. Krieger, Photochemical degradation of iron(III) citrate/citric acid aerosol quantified with the combination of three complementary experimental techniques and a kinetic process model, *Atmos. Chem. Phys.*, 2021, **21**, 315–338.

37 N. M. Garner, F. Mahrt, J. Top, V. Tadei, K. Kilchhofer, S. Takahama, I. El Haddad, D. M. Bell, M. Ammann and P. A. Alpert, Photochemistry of iron-containing secondary organic aerosol is impacted by relative humidity during formation, *npj Clim. Atmos. Sci.*, 2025, **8**, 246.

38 Y. Gou, M. Xie and J. Chen, The phase state and viscosity of organic aerosol and related impacts on atmospheric physicochemical processes: A review, *Atmos. Environ.*, 2025, **343**, 120985.

39 J. P. Reid, A. K. Bertram, D. O. Topping, A. Laskin, S. T. Martin, M. D. Petters, F. D. Pope and G. Rovelli, The viscosity of atmospherically relevant organic particles, *Nat. Commun.*, 2018, **9**, 956.

40 L. Renbaum-Wolff, J. W. Grayson and A. K. Bertram, Technical Note: New methodology for measuring viscosities in small volumes characteristic of environmental chamber particle samples, *Atmos. Chem. Phys.*, 2013, **13**, 791–802.

41 K. J. Kiland, K. L. Marroquin, N. R. Smith, S. Xu, S. A. Nizkorodov and A. K. Bertram, A new hot-stage microscopy technique for measuring temperature-dependent viscosities of aerosol particles and its application to farnesene secondary organic aerosol, *Atmos. Meas. Tech.*, 2022, **15**, 5545–5561.

42 R. M. Power, S. H. Simpson, J. P. Reid and A. J. Hudson, The transition from liquid to solid-like behaviour in ultrahigh viscosity aerosol particles, *Chem. Sci.*, 2013, **4**, 2597–2604.

43 H. D. Lee, K. K. Ray and A. V. Tivanski, Solid, Semisolid, and Liquid Phase States of Individual Submicrometer Particles Directly Probed Using Atomic Force Microscopy, *Anal. Chem.*, 2017, **89**, 12720–12726.

44 H. D. Lee and A. V. Tivanski, Atomic Force Microscopy: An Emerging Tool in Measuring the Phase State and Surface Tension of Individual Aerosol Particles, *Annu. Rev. Phys. Chem.*, 2021, **72**, 235–252.

45 C. K. Madawala, H. D. Lee, C. P. Kaluarachchi and A. V. Tivanski, Quantifying the Viscosity of Individual Submicrometer Semisolid Particles Using Atomic Force Microscopy, *Anal. Chem.*, 2023, **95**, 14566–14572.

46 Z. Lei, J. Zhang, E. A. Mueller, Y. Xiao, K. R. Kolozsvari, A. J. McNeil, M. M. Banaszak Holl and A. P. Ault, Glass Transition Temperatures of Individual Submicrometer Atmospheric Particles: Direct Measurement via Heated Atomic Force Microscopy Probe, *Anal. Chem.*, 2022, **94**, 11973–11977.

47 K. R. A. Kolozsvari, C. M. Waters, J. Yan, N. C. Armstrong, A. M. Fankhauser, M. E. Cooke, Y. Xiao, R. L. Parham, M. Frauenheim, Z. Zhang, A. Gold, J. D. Surratt and A. P. Ault, Single-Particle Viscosity of Isoprene-Derived Secondary Organic Aerosol Formed across a Range of Relative Humidities and Aging Conditions Reveals

Morphology-Dependent Effects, *Environ. Sci. Technol.*, 2025, **59**, 23386–23397.

48 W.-S. W. DeRieux, Y. Li, P. Lin, J. Laskin, A. Laskin, A. K. Bertram, S. A. Nizkorodov and M. Shiraiwa, Predicting the glass transition temperature and viscosity of secondary organic material using molecular composition, *Atmos. Chem. Phys.*, 2018, **18**, 6331–6351.

49 Y. Li, D. A. Day, H. Stark, J. L. Jimenez and M. Shiraiwa, Predictions of the glass transition temperature and viscosity of organic aerosols from volatility distributions, *Atmos. Chem. Phys.*, 2020, **20**, 8103–8122.

50 S. M. Platt, I. El Haddad, A. A. Zardini, M. Clairotte, C. Astorga, R. Wolf, J. G. Slowik, B. Temime-Roussel, N. Marchand, I. Ježek, L. Drinovec, G. Močnik, O. Möhler, R. Richter, P. Barmet, F. Bianchi, U. Baltensperger and A. S. H. Prévôt, Secondary organic aerosol formation from gasoline vehicle emissions in a new mobile environmental reaction chamber, *Atmos. Chem. Phys.*, 2013, **13**, 9141–9158.

51 V. Pospisilova, D. M. Bell, H. Lamkaddam, A. Bertrand, L. Wang, D. Bhattu, X. Zhou, J. Dommen, A. S. H. Prevot, U. Baltensperger, I. El Haddad and J. G. Slowik, Photodegradation of α-Pinene Secondary Organic Aerosol Dominated by Moderately Oxidized Molecules, *Environ. Sci. Technol.*, 2021, **55**, 6936–6943.

52 O. Laskina, H. S. Morris, J. R. Grandquist, A. D. Estillore, E. A. Stone, V. H. Grassian and A. V. Tivanski, Substrate-Deposited Sea Spray Aerosol Particles: Influence of Analytical Method, Substrate, and Storage Conditions on Particle Size, Phase, and Morphology, *Environ. Sci. Technol.*, 2015, **49**, 13447–13453.

53 F. D. Lopez-Hilfiker, V. Pospisilova, W. Huang, M. Kalberer, C. Mohr, G. Stefenelli, J. A. Thornton, U. Baltensperger, A. S. H. Prevot and J. G. Slowik, An extractive electrospray ionization time-of-flight mass spectrometer (EESI-TOF) for online measurement of atmospheric aerosol particles, *Atmos. Meas. Tech.*, 2019, **12**, 4867–4886.

54 D. S. Wang, C. P. Lee, J. E. Krechmer, F. Majluf, Y. Tong, M. R. Canagaratna, J. Schmale, A. S. H. Prévôt, U. Baltensperger, J. Dommen, I. El Haddad, J. G. Slowik and D. M. Bell, Constraining the response factors of an extractive electrospray ionization mass spectrometer for near-molecular aerosol speciation, *Atmos. Meas. Tech.*, 2021, **14**, 6955–6972.

55 R. G. Beaman, Relation between (apparent) second-order transition temperature and melting point, *J. Polym. Sci.*, 1952, **9**, 470–472.

56 M. Shiraiwa, Y. Li, A. P. Tsimpidi, V. A. Karydis, T. Berkemeier, S. N. Pandis, J. Lelieveld, T. Koop and U. Pöschl, Global distribution of particle phase state in atmospheric secondary organic aerosols, *Nat. Commun.*, 2017, **8**, 15002.

57 T. B. Nguyen, S. A. Nizkorodov, A. Laskin and J. Laskin, An approach toward quantification of organic compounds in complex environmental samples using high-resolution electrospray ionization mass spectrometry, *Anal. Methods*, 2012, **5**, 72–80.

58 N. E. Rothfuss and M. D. Petters, Characterization of the temperature and humidity-dependent phase diagram of amorphous nanoscale organic aerosols, *Phys. Chem. Chem. Phys.*, 2017, **19**, 6532–6545.

59 E. Mikhailov, S. Vlasenko, D. Rose and U. Pöschl, Mass-based hygroscopicity parameter interaction model and measurement of atmospheric aerosol water uptake, *Atmos. Chem. Phys.*, 2013, **13**, 717–740.

60 C. A. Angell, Liquid Fragility and the Glass Transition in Water and Aqueous Solutions, *Chem. Rev.*, 2002, **102**, 2627–2650.

61 C. A. Angell, Relaxation in liquids, polymers and plastic crystals — strong/fragile patterns and problems, *J. Non-Cryst. Solids*, 1991, **131–133**, 13–31.

62 P. C. Arroyo, K. T. Malecha, M. Ammann and S. A. Nizkorodov, Influence of humidity and iron(iii) on photodegradation of atmospheric secondary organic aerosol particles, *Phys. Chem. Chem. Phys.*, 2018, **20**, 30021–30031.

63 W. Li, L. Liu, J. Zhang, L. Xu, Y. Wang, Y. Sun and Z. Shi, Microscopic Evidence for Phase Separation of Organic Species and Inorganic Salts in Fine Ambient Aerosol Particles, *Environ. Sci. Technol.*, 2021, **55**, 2234–2242.

64 K. A. Pratt and K. A. Prather, Real-Time, Single-Particle Volatility, Size, and Chemical Composition Measurements of Aged Urban Aerosols, *Environ. Sci. Technol.*, 2009, **43**, 8276–8282.

65 A. M. Middlebrook, D. M. Murphy and D. S. Thomson, Observations of organic material in individual marine particles at Cape Grim during the First Aerosol Characterization Experiment (ACE 1), *J. Geophys. Res.:Atmos.*, 1998, **103**, 16475–16483.

66 D. M. Murphy, D. J. Cziczo, K. D. Froyd, P. K. Hudson, B. M. Matthew, A. M. Middlebrook, R. E. Peltier, A. Sullivan, D. S. Thomson and R. J. Weber, Single-particle mass spectrometry of tropospheric aerosol particles, *J. Geophys. Res.:Atmos.*, 2006, **111**, D23S32.

67 R. M. Kirpes, Z. Lei, M. Fraund, M. J. Gunsch, N. W. May, T. E. Barrett, C. E. Moffett, A. J. Schauer, B. Alexander, L. M. Upchurch, S. China, P. K. Quinn, R. C. Moffet, A. Laskin, R. J. Sheesley, K. A. Pratt and A. P. Ault, Solid organic-coated ammonium sulfate particles at high relative humidity in the summertime Arctic atmosphere, *Proc. Natl. Acad. Sci. U. S. A.*, 2022, **119**, e2104496119.